Influence of grain morphology and orientation on the elastic and magnetoelastic properties of polycrystalline Terfenol-D

P. Nieves[a,*], D. Legut[a]

[a] *IT4Innovations, VŠB - Technical University of Ostrava, 17. listopadu 2172/15, 70800 Ostrava-Poruba, Czech Republic*

Abstract

In this work we computationally simulate the effect of microstructure on elastic and magnetostrictive properties of Terfenol-D ($Tb_{0.27}Dy_{0.73}Fe_2$) by means of Finite Element Method. The simulations successfully reproduce the theoretical and experimental Young's modulus and magnetostrictive coefficient of polycrystalline Terfenol-D. In the linear elastic regime, the crystal orientation distribution of the grains produces a greater influence on the properties than the morphology of the grains. A correlation between the dispersion angle of the oriented growth crystal directions ($< 011 >$ and $< 111 >$) and magnetoelastic performance is obtained. At low dispersion angles, an effective macroscopic uniaxial magnetocrystalline anisotropy is found along the oriented growth crystal direction.

Keywords: Magnetostriction, Magnetoelasticity, Elasticity, Magnetocrystalline anisotropy, Polycrystal, Finite element method

1. Introduction

Terfenol-D ($Tb_{0.27}Dy_{0.73}Fe_2$) is a compound with Laves phase C15 structure type (face centered cubic) that exhibits a giant magnetostriction along $< 111 >$ crystallographic direction ($\lambda_{111} = 1.6 \times 10^{-3}$) under moderate magnetic fields (< 2 kOe) at room temperature [1]. Presently, this material is commercially used in many types of sensors and actuators [2]. While single-crystal magnetostrictive alloys are easier to understand and characterize, polycrystals are more

*Corresponding author.
E-mail address: pablo.nieves.cordones@vsb.cz

suitable for macroscale applications due to lower production cost and faster production rate. The elastic and magnetoelastic properties of polycrystals can be significantly influenced by many factors, such as crystal orientation, orientation degree, microstructure and crystal defects. For instance, the low magnetostriction along the crystallographic direction $< 100 >$ ($\lambda_{100} = 9 \times 10^{-5}$) of Terfenol-D reduces the magnetostriction up to $\lambda_s \simeq \frac{2}{3}\lambda_{111}$ in polycrystalline samples with randomly oriented grains. Similarly, these samples exhibit a moderate Young's modulus (110 GPa) that might limit the range of applicability of Terfenol-D, especially to support large forces under extreme conditions [2]. The orientation of the grains in some specific crystallographic directions could be a convenient strategy to tune and enhance the elastic and magnetoelastic properties of polycrystalline Terfenol-D [3]. Wang et al. investigated Terfenol-D polycrystals with $< 110 >$ axial alignment finding excellent magnetostrictive properties under low magnetic fields [4]. Kown et al. studied the effect of texture on the magnetostriction of grain-aligned composite Terfenol-D and confirmed that the effective magnetostriction depends on the preferred growth direction [5, 6]. Concerning the preparation of grain-aligned samples, Ji et al. achieved highly oriented grains in $< 110 >$ with dispersion angle of only 3^o using a temperature gradient directional solidification technique [7]. In this work, we computationally study the influence of grain morphology and orientation on the elastic and magnetoelastic properties of polycrystalline Terfenol-D by means of Finite Element Method (FEM).

2. Methodology

2.1. Theoretical equations

In this work we perform a linear static analysis of the deformation induced by external mechanical forces or magnetic field to compute the elastic and magnetoelastic properties. The deformation is given by the displacement vector $\boldsymbol{u}(\boldsymbol{r}) = \boldsymbol{r'} - \boldsymbol{r}$ that gives the displacement from a point at the initial position $\boldsymbol{r}$ to its final position $\boldsymbol{r'}$. For small deformations, the displacement vector can be calculated by solving [8]

$$\varepsilon_{ij} = \frac{1}{2}\left(\frac{\partial u_i}{\partial r_j} + \frac{\partial u_j}{\partial r_i}\right), \qquad i,j = x,y,z \tag{1}$$

where ε_{ij} is the strain tensor. Hence, one needs to provide the strain tensor as input in Eq.1 in order to compute the deformation through the displacement vector $\boldsymbol{u}$. To calculate elastic properties like the Young's modulus, we obtain the strain tensor by solving the stress-strain equations. On the other hand, to compute

magnetostriction we directly use the theoretical equilibrium magnetoelastic strain tensor that is derived from the minimization of the elastic and magnetoelastic energies. In the following two sections, we explain in more detail how the strain tensor is calculated for each case.

2.1.1. Elastic properties

To calculate the elastic properties, we apply external mechanical forces on some specific boundaries of the material and compute the equilibrium strain tensor by solving the stress-strain equations

$$\begin{pmatrix} \sigma_{xx} \\ \sigma_{yy} \\ \sigma_{zz} \\ \sigma_{yz} \\ \sigma_{xz} \\ \sigma_{xy} \end{pmatrix} = \begin{pmatrix} C_{11} & C_{12} & C_{13} & C_{14} & C_{15} & C_{16} \\ C_{21} & C_{22} & C_{23} & C_{24} & C_{25} & C_{26} \\ C_{31} & C_{32} & C_{33} & C_{34} & C_{35} & C_{36} \\ C_{41} & C_{42} & C_{42} & C_{44} & C_{45} & C_{46} \\ C_{51} & C_{52} & C_{53} & C_{54} & C_{55} & C_{56} \\ C_{61} & C_{62} & C_{63} & C_{64} & C_{65} & C_{66} \end{pmatrix} \begin{pmatrix} \varepsilon_{xx} \\ \varepsilon_{yy} \\ \varepsilon_{zz} \\ 2\varepsilon_{yz} \\ 2\varepsilon_{xz} \\ 2\varepsilon_{xy} \end{pmatrix}, \tag{2}$$

where σ_{ij} is the stress tensor and C_{ij} is the elastic tensor. We additionally assume that our material is hyperelastic (there exists an elastic energy function) what implies that $C_{ij} = C_{ji}$. Moreover, since Terfenol-D is a cubic crystal the elastic tensor is further reduced to

$$C = \begin{pmatrix} C_{11} & C_{12} & C_{12} & 0 & 0 & 0 \\ C_{12} & C_{11} & C_{12} & 0 & 0 & 0 \\ C_{12} & C_{12} & C_{11} & 0 & 0 & 0 \\ 0 & 0 & 0 & C_{44} & 0 & 0 \\ 0 & 0 & 0 & 0 & C_{44} & 0 \\ 0 & 0 & 0 & 0 & 0 & C_{44} \end{pmatrix}, \tag{3}$$

so there are only three independent elastic constants C_{11}, C_{12} and C_{44}. The form of the elastic tensor in Eq.3 corresponds to a cubic crystal with crystallographic axis $< 100 >$, $< 010 >$ and $< 001 >$ along the cartesian X, Y and Z axis, respectively. If we perform an active rotation of the crystal with Euler angles (ϕ, θ, ψ) in Bunge convention Z-X-Z, then elastic tensor is transformed as[9]

$$C''' = M(\psi)M'(\theta)M(\phi)C\tilde{M}(\phi)\tilde{M}'(\theta)\tilde{M}(\psi), \tag{4}$$

where

$$M(\phi) = \begin{pmatrix} cos^2(\phi) & sin^2(\phi) & 0 & 0 & 0 & -sin(2\phi) \\ sin^2(\phi) & cos^2(\phi) & 0 & 0 & 0 & sin(2\phi) \\ 0 & 0 & 1 & 0 & 0 & 0 \\ 0 & 0 & 0 & cos(\phi) & sin(\phi) & 0 \\ 0 & 0 & 0 & -sin(\phi) & cos(\phi) & 0 \\ \frac{1}{2}sin(2\phi) & \frac{-1}{2}sin(2\phi) & 0 & 0 & 0 & cos(2\phi) \end{pmatrix},$$
$$M'(\theta) = \begin{pmatrix} 1 & 0 & 0 & 0 & 0 & 0 \\ 0 & cos^2(\theta) & sin^2(\theta) & -sin(2\theta) & 0 & 0 \\ 0 & sin^2(\theta) & cos^2(\theta) & sin(2\theta) & 0 & 0 \\ 0 & \frac{1}{2}sin(2\theta) & \frac{-1}{2}sin(2\theta) & cos(2\theta) & 0 & 0 \\ 0 & 0 & 0 & 0 & cos(\theta) & sin(\theta) \\ 0 & 0 & 0 & 0 & -sin(\theta) & cos(\theta) \end{pmatrix}. \quad (5)$$

The matrices $\tilde{M}$ and $\tilde{M}'$ are the transpose of matrices M and M', respectively.

2.1.2. Magnetoelastic properties

To compute magnetostriction, we make use of the equilibrium magnetoelastic strain tensor that can be analytically derived from the minimization of both the elastic and magnetoelastic energies [10, 11]. For a cubic single crystal (point groups 432, $\bar{4}3m$, $m\bar{3}m$) equilibrium magnetoelastic strain tensor reads [10, 11]

$$\varepsilon(\boldsymbol{\alpha}) = \begin{pmatrix} \lambda^{\alpha} + \frac{3}{2}\lambda_{001}\left(\alpha_{100}^2 - \frac{1}{3}\right) & \frac{3}{2}\lambda_{111}\alpha_{100}\alpha_{010} & \frac{3}{2}\lambda_{111}\alpha_{100}\alpha_{001} \\ \frac{3}{2}\lambda_{111}\alpha_{100}\alpha_{010} & \lambda^{\alpha} + \frac{3}{2}\lambda_{001}\left(\alpha_{010}^2 - \frac{1}{3}\right) & \frac{3}{2}\lambda_{111}\alpha_{010}\alpha_{001} \\ \frac{3}{2}\lambda_{111}\alpha_{100}\alpha_{001} & \frac{3}{2}\lambda_{111}\alpha_{010}\alpha_{001} & \lambda^{\alpha} + \frac{3}{2}\lambda_{001}\left(\alpha_{001}^2 - \frac{1}{3}\right) \end{pmatrix}, \quad (6)$$

where λ^{α} describes the isotropic magnetostriction, while λ_{001} and λ_{111} are the anisotropic magnetostrictive coefficients that give the fractional length change along the $< 001 >$ and $< 111 >$ crystallographic directions when a demagnetized material is magnetized in these directions, respectively. The vector $\boldsymbol{\alpha} = (\alpha_{100}, \alpha_{010}, \alpha_{001})$ gives the reduced magnetization (saturated magnetic state) with respect to the crystal axis, that is, the quantities α_{100}, α_{010} and α_{001} denote the components of the reduced magnetization along the crystallographic directions $< 001 >$, $< 010 >$ and $< 001 >$, respectively. The form of the magnetoelastic strain tensor in Eq.6 corresponds to a cubic crystal with crystallographic axis $< 100 >$, $< 010 >$ and $< 001 >$ along the cartesian X, Y and Z axis, respectively. If we perform an active rotation of the crystal with Euler angles (ϕ, θ, ψ) in Bunge

convention Z-X'-Z'', then the magnetoelastic strain tensor is transformed as[9]

$$\varepsilon'''(\boldsymbol{\alpha}) = N(\psi)N'(\theta)N(\phi)\varepsilon(\boldsymbol{\alpha})\tilde{N}(\phi)\tilde{N}'(\theta)\tilde{N}(\psi), \tag{7}$$

where

$$\begin{aligned} N(\phi) &= \begin{pmatrix} cos(\phi) & -sin(\phi) & 0 \\ sin(\phi) & cos(\phi) & 0 \\ 0 & 0 & 1 \end{pmatrix}, \\ N'(\theta) &= \begin{pmatrix} 1 & 0 & 0 \\ 0 & cos(\theta) & -sin(\theta) \\ 0 & sin(\theta) & cos(\theta) \end{pmatrix}. \end{aligned} \tag{8}$$

The matrices $\tilde{N}$ and $\tilde{N}'$ are the transpose of matrices N and N', respectively. In Fig. 1 we illustrate this transformation. Additionally, if in this rotated grain we set the reduced magnetization $\boldsymbol{m} = (m_x, m_y, m_z)$ with respect to the cartesian axis X, Y and Z, then the reduced magnetization with respect to the crystallographic axis is given by

$$\boldsymbol{\alpha} = N(-\phi)N'(-\theta)N(-\psi)\boldsymbol{m}. \tag{9}$$

This conversion formula is useful for the evaluation of magnetoelastic strain tensor of each rotated grain in a polycrystalline materials since the magnetization of all grains are typically saturated to a particular direction with respect to the cartesian coordinates X, Y and Z of the all material.

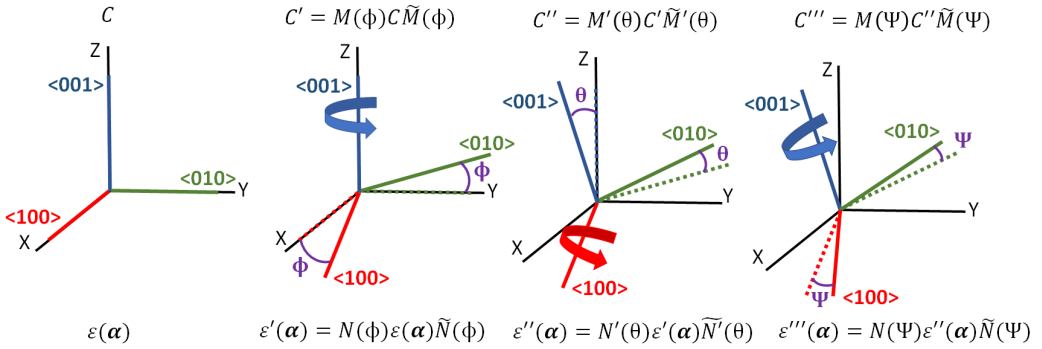

Figure 1: Transformation of the elastic tensor (C) and magnetoelastic strain tensor (ε) when an active rotation of the crystal is performed with Euler angles (ϕ, θ, ψ) in Bunge convention.

The magnetocrystalline anisotropy energy E_K of an unstrained cubic crystal is [12, 13]

$$\frac{E_K(\boldsymbol{\alpha})}{V_0} = K_1(\alpha_{100}^2\alpha_{010}^2 + \alpha_{100}^2\alpha_{001}^2 + \alpha_{010}^2\alpha_{001}^2) + K_2\alpha_{100}^2\alpha_{010}^2\alpha_{001}^2, \tag{10}$$

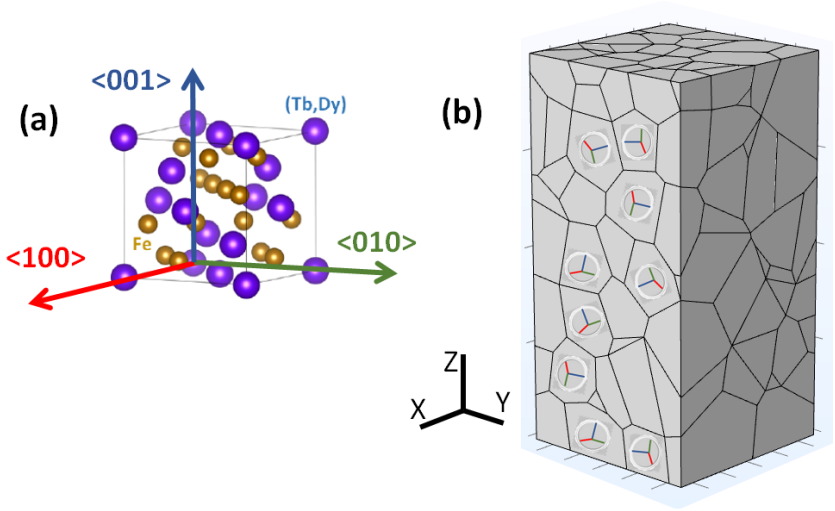

Figure 2: (a) Single crystal of Terfenol-D. (b) Polycrystalline model of Terfenol-D where the crystallographic axis of some grains are depicted.

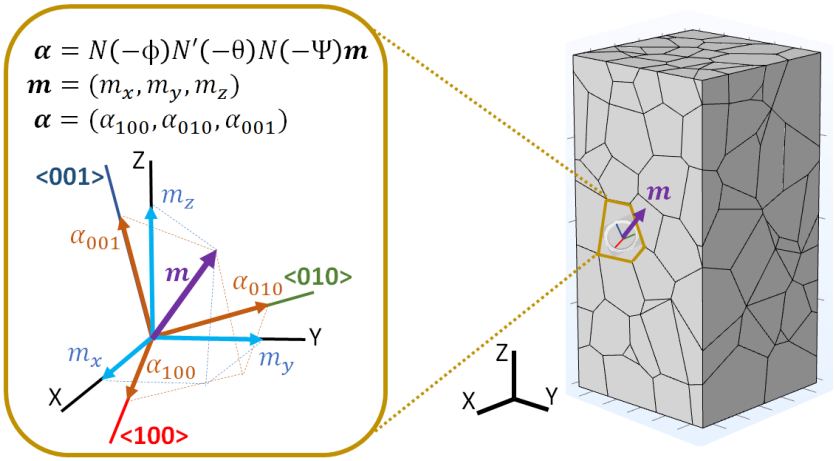

Figure 3: Diagram showing the components of the reduced magnetization vector ($\boldsymbol{m}$) for a particular grain inside the polycrystalline material. The components of the reduced magnetization are shown in the global polycrystalline material's coordinates XYZ (m_x, m_y, m_z) and rotated crystallographic axis ($\alpha_{100}, \alpha_{010}, \alpha_{001}$). The grain is actively rotated with Euler angles (ϕ, θ, ψ) in Bunge convention, as depicted in Fig.1.

where K_1 and K_2 are the magnetocrystalline anisotropy constants, and V_0 is the volume of the grain.

Table 1: Properties used in the model of Terfenol-D at room temperature.

Material	Temperature (K)	C_{11} (GPa)	C_{12} (GPa)	C_{44} (GPa)	λ^{α} ($\times 10^{-6}$)	λ_{001} ($\times 10^{-6}$)	λ_{111} ($\times 10^{-6}$)	K_1 (MJ/m^3)	K_2 (KJ/m^3)
Terfenol-D	300	141[a]	64.8[a]	48.7[a]	0[b]	1600[c]	90[c]	-40[d]	-100[d]

[a]Ref.[10, 14], [b]Ref.[16], [c]Ref.[2], [d]Ref.[17]

2.2. Properties of Terfenol-D

2.2.1. Bulk

In this work we study Terfenol-D at room temperature. For the elastic constants we set the values given by Clark [10, 14] $C_{11} = 141$ GPa, $C_{12} = 64.8$ GPa and $C_{44} = 48.7$ GPa. Robillard et al. used a smaller value for C_{11} ($C_{11} = 82$GPa) to model a commercial sample of Terfenol-D [15]. Concerning anisotropic magnetostrictive constants, we use the values given by Dapino [2] $\lambda_{001} = 90 \times 10^{-6}$ and $\lambda_{111} = 1600 \times 10^{-6}$. Arnaudas et al. reported that the magnetoelastic constant associated to volume magnetostriction is negligible ($b_0 \leq 2$MPa, $|b_1| \gg |b_0|$, $|b_2| \gg |b_0|$) [16], so that we set the isotropic magnetostrictive coefficient to zero ($\lambda^{\alpha} = 0$). The magnetocrystalline anisotropy constants vary significantly, depending on temperature and stoichiometry [2, 14, 16, 17]. In this model we use the values $K_1 = -40$KJ/m^3 and $K_2 = -100$KJ/m^3 that were reported by Teter et al. from deviations from the cosine dependence of the low magnetic field values of magnetostriction versus angle [17]. In Table 1 we summarize the values used in the model of Terfenol-D at room temperature.

2.2.2. Grain boundaries

The modeling and understanding of elastic and magnetoelastic phenomenology at grain boundaries is difficult due to the complexity and diversity of these regions in a polycrystalline material. In the present model we consider that all points of the grain, including point close to grain boundaries, are described by the bulk properties shown in Table 1. This approximation might be reasonable to roughly estimate properties of polycrystalline materials originated mainly from the bulk region of the grains. For instance, if the volume occupied by the bulk region of the grains is much larger than the volume occupied by grain boundaries, then one might expect that the overall deformation (under external force or magnetic field) and total magnetocrystalline anisotropy energy should mainly given by the bulk region of the grains. To make a quick estimation, let's consider a spherical grain with radius R surrounded by a thin shell with thickness δR that contains the grain boundary. The ratio between the volume of the grain and the

grain boundary is $V_{Grain}/V_{Shell} = R/(3\delta R)$. Typically, as one moves away from the grain boundaries, local atomic properties rapidly converge to bulk properties so for this example we could assume a thin grain boundary region $\delta R \sim 1$nm. In this work, we consider microstructures with grain size $R \sim 1\mu$m (see Fig.17) so that the main contribution to the studied properties here might be given by the bulk region of the grains. Note that this approach might fail in nanocrystalline alloys [18] where the volume occupied by the bulk region of the grains and grain boundaries are comparable. We point out that even in microstructures with micrometer grain sizes the grain boundaries could also influence significantly some properties like coercivity by pinning or nueclating magnetic domains [19].

2.3. Numerical methods

The equations described in Section 2.1 are solved by means of Finite Element Model (FEM) techniques as implemented in the software COMSOL[20] interfaced with MATLAB[21]. In the simulations we used a tetrahedral mesh and the direct method PARDISO to solve the linear systems of equations with default settings of COMSOL (version 5.6). The generation of the polycrystalline models and nearly uniform sampling of crystal orientations (Euler angles, active rotation in Bunge convention) are performed with software Neper [22, 23]. Once the deformation of the system is calculated, the change in length ΔL in the z-axis direction is calculated as the spatial average of the z-component of the displacement vector (u_z) on the top boundary Σ

$$< \Delta L_z > = < L_z - L_{z,0} > = \frac{\int_\Sigma u_z(x,y,L_{z,0})dxdy}{\int_\Sigma dxdy}, \tag{11}$$

where L_{0_z} is the initial length in the z-axis direction before deformation takes place. A fixed constraint is imposed at the bottom boundary $u_z(x,y,0) = 0$ for reference purposes. Eq.11 is numerically computed with the analysis tools implemented in COMSOL [20]. Next, the Young's modulus is obtained via $Y = PL_{z,0}/ < \Delta L_z >$, where P is the external pressure applied at the bottom and top boundaries of the system in the FEM simulation. Similarly, magnetostriction is calculated as $\lambda = < \Delta L_z > /L_{z,0}$, where L_{0_z} is the length in the z-axis direction in the demagnetized state.

3. Results

3.1. Single crystal

Before we study the polycrystalline material, it is convenient to check the implementation of the methodology described in Section 2 using only a single crystal

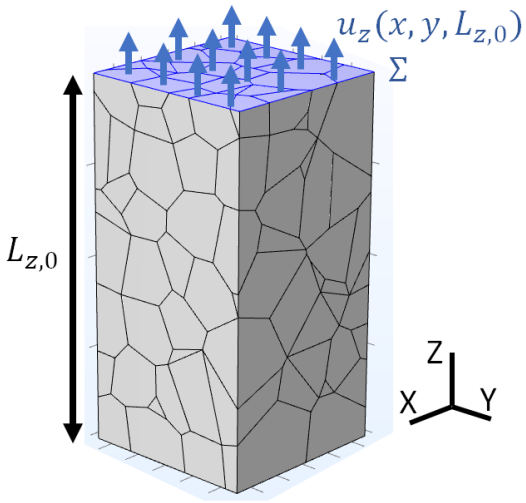

Figure 4: Scheme showing the calculation of the change in length along the z-axis for the polycrystalline model of Terfenol-D.

grain. To do so, we verify that the Young's modulus and magnetostriction of a rotated single crystal Terfenol-D calculated by FEM simulation is in agreement with theory.

3.1.1. Young's modulus

The theoretical expression for the Young's modulus along the crystallographic direction given by the spherical coordinates

$$\boldsymbol{a}(\theta',\phi') = \begin{pmatrix} a_1 \\ a_2 \\ a_3 \end{pmatrix} = \begin{pmatrix} sin\theta' cos\phi' \\ sin\theta' sin\phi' \\ cos\theta' \end{pmatrix}, \tag{12}$$

is [24, 25]

$$Y(\theta',\phi') = \left[\sum_{i,j,k,l=1}^{3} a_i a_j a_k a_l S_{ijkl} \right]^{-1}, \tag{13}$$

where S_{ijkl} is the fourth rank compliance tensor that is the inverse of the elastic tensor $S = C^{-1}$. For instance, the Young's modulus of a cubic crystal along the crystallographic direction with $\theta' = \pi/2$ is given by

$$Y\left(\frac{\pi}{2},\phi'\right) = \frac{4}{S_{11}(3+cos(4\phi')) + (2S_{12}+S_{44})sin^2(2\phi')}, \tag{14}$$

where

$$S_{11} = \frac{C_{11}+C_{12}}{(C_{11}-C_{12})(C_{11}+2C_{12})}, \tag{15}$$

$$S_{12} = \frac{-C_{12}}{(C_{11}-C_{12})(C_{11}+2C_{12})}, \tag{16}$$

$$S_{44} = \frac{1}{C_{44}}. \tag{17}$$

Now, let's apply the methodology described in Section 2.1.1 to compute the Young's modulus via FEM, and compare the result with the theoretical value given by Eq.14. For this simulation we consider a rectangular grain with initial length $L_{x,0} = 20\mu$m and $L_{y,0} = L_{z,0} = 10\mu$m. We apply an external negative pressure $P = -0.1$GPa on both boundaries parallel to the YZ plane, so the material will expand in the X-direction. We take into account the crystallographic orientation of the crystal by transforming the elastic tensor via Eq. 4, where the Euler angles are $\phi = -\phi'$, $\theta = 0$ and $\psi = 0$. Once the deformation is computed by solving the stress-strain equations with COMSOL, the Young's modulus is obtained using the expression $Y = PL_{x,0}/ < \Delta L_x >$, where $< \Delta L_x >$ is calculated as the spatial average of the x-component of the displacement vector (u_x) at the boundary Σ with points $\boldsymbol{r} = (L_{x,0}, y, z)$, that is

$$< \Delta L_x > = < L_x - L_{x,0} > = \frac{\int_\Sigma u_x(L_{x,0}, y, z)dydz}{\int_\Sigma dydz}. \tag{18}$$

The model setup is depicted in Fig.5. The results for the Young's modulus along the crystallographic direction $\boldsymbol{a} = (cos\phi', sin\phi', 0)$ calculated with FEM and Eq. 14 are shown in Fig. 6. We see that the simulation with FEM is in very good agreement with the theory, ensuring the correct implementation of the methodology described in Section 2.1.1. Similar tests can also be performed along other crystallographic direction $\boldsymbol{a}$.

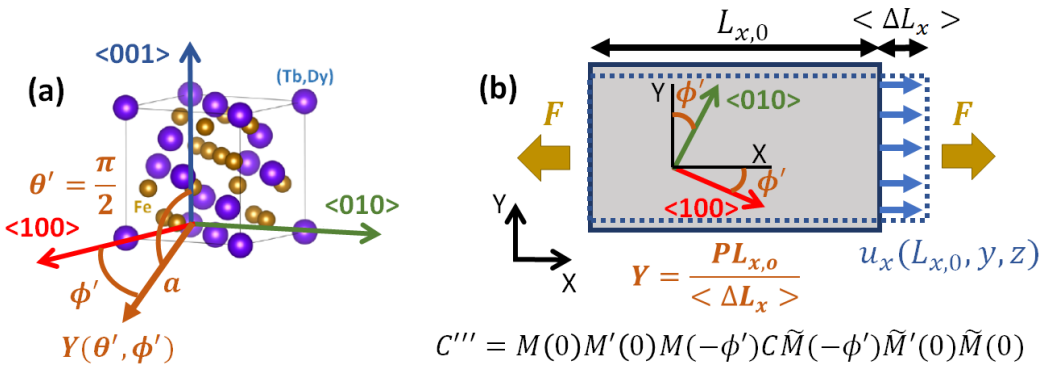

Figure 5: Scheme showing the calculation of the Young's modulus for a single crystal of Terfenol-D along the crystallographic direction $\boldsymbol{a} = (cos\phi', sin\phi', 0)$.

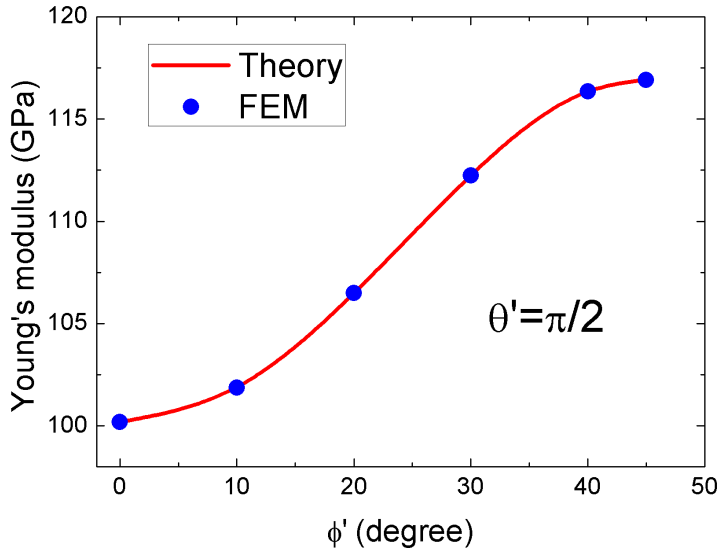

Figure 6: Calculation of the Young's modulus for a single crystal of Terfenol-D along the crystallographic direction $\boldsymbol{a} = (cos\phi', sin\phi', 0)$ using FEM (blue dots) and Eq.14 (red line).

3.1.2. Magnetostriction

The relative length change for a cubic single crystal system (point groups 432, $\bar{4}3m$, $m\bar{3}m$) can be written as [11]

$$\begin{aligned}\left.\frac{\Delta l}{l_0}\right|_{\boldsymbol{\beta}}^{\boldsymbol{\alpha}} &= \lambda^{\alpha} + \frac{3}{2}\lambda_{001}\left(\alpha_{100}^2\beta_{100}^2 + \alpha_{010}^2\beta_{010}^2 + \alpha_{001}^2\beta_{001}^2 - \frac{1}{3}\right) \\ &+ 3\lambda_{111}(\alpha_{100}\alpha_{010}\beta_{100}\beta_{010} + \alpha_{010}\alpha_{001}\beta_{010}\beta_{001} + \alpha_{100}\alpha_{001}\beta_{100}\beta_{001}) \\ &= \lambda^{\alpha} + \frac{3}{2}\lambda_{001}\left(m_x^2\beta'^2_x + m_y^2\beta'^2_y + m_z^2\beta'^2_z - \frac{1}{3}\right) \\ &+ 3\lambda_{111}(m_x m_y \beta'_x\beta'_y + m_y m_z \beta'_y\beta'_z + m_x m_z \beta'_x\beta'_z)\end{aligned} \tag{19}$$

where $\boldsymbol{\beta} = (\beta_{100}, \beta_{010}, \beta_{001})$ is an unit vector ($|\boldsymbol{\beta}| = 1$) that describes the measuring length direction with respect to the crystal axis, that is, the quantities β_{100}, β_{010} and β_{001} denote the components of the measuring length direction along the crystallographic directions $< 001 >$, $< 010 >$ and $< 001 >$, respectively. The vector $\boldsymbol{\beta}' = (\beta'_x, \beta'_y, \beta'_z)$ is a unit vector that describes the measuring length direction in the global cartesian coordinates XYZ of the material. The vectors $\boldsymbol{\beta}$ and $\boldsymbol{\beta}'$ are related to each other in the same way as $\boldsymbol{\alpha}$ and $\boldsymbol{m}$ (Eq.9), that is

$$\boldsymbol{\beta} = N(-\phi)N'(-\theta)N(-\psi)\boldsymbol{\beta}'. \tag{20}$$

For instance, if we consider the particular case $\boldsymbol{\alpha} = (cos(\eta), sin(\eta), 0)$ and $\boldsymbol{\beta} = (cos(-\gamma), sin(-\gamma), 0)$, then Eq.19 becomes

$$\begin{aligned}\left.\frac{\Delta l}{l_0}\right|_{\boldsymbol{\beta}}^{\boldsymbol{\alpha}} &= \lambda^{\alpha} + \frac{3}{2}\lambda_{001}\left(cos^2(\eta)cos^2(-\gamma) + sin^2(\eta)sin^2(-\gamma) - \frac{1}{3}\right) \\ &+ 3\lambda_{111}cos(\eta)sin(\eta)cos(-\gamma), sin(-\gamma).\end{aligned} \tag{21}$$

Now, let's apply the methodology described in Section 2.1.2 to compute the relative length change via FEM, and compare the result with the theoretical value given by Eq.21. For this simulation we consider again a rectangular grain with initial length $L_{x,0} = 20\mu$m and $L_{y,0} = L_{z,0} = 10\mu$m. We take into account the crystallographic orientation of the crystal by transforming the magnetoelastic strain tensor via Eq. 6, where the Euler angles are $\phi = \gamma$, $\theta = 0$ and $\psi = 0$. The reduced magnetization with respect to the material cartesian coordinates is $\boldsymbol{m} = (cos(\eta + \gamma), sin(\eta + \gamma), 0)$. The model setup is depicted in Fig.7. Once the deformation is computed by solving Eq.1 with COMSOL, the relative length change in

the x-direction is obtained using the expression $< \Delta L_x > / L_{x,0}$, where $< \Delta L_x >$ is calculated via Eq.18. The results for the relative length change along the crystallographic direction $\boldsymbol{\beta} = (cos(-\gamma), sin(-\gamma), 0)$ with $\eta = 40^o$ calculated with FEM and Eq. 21 are shown in Fig. 8. We see that the simulation with FEM is in very good agreement with the theory, ensuring the correct implementation of the methodology described in Section 2.1.2. Similar tests can also be performed choosing other values for $\boldsymbol{\alpha}$ and $\boldsymbol{\beta}$.

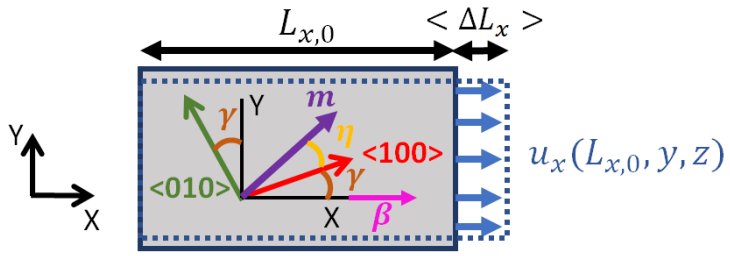

$$\boldsymbol{m} = (\cos(\eta + \gamma), \sin(\eta + \gamma), 0)$$

$$\boldsymbol{\alpha} = N(-\gamma)N'(0)N(0)\boldsymbol{m}$$

$$\varepsilon'''(\boldsymbol{\alpha}) = N(0)N'(0)N(\gamma)\varepsilon(\boldsymbol{\alpha})\widetilde{N}(\gamma)\widetilde{N'}(0)\widetilde{N}(0)$$

Figure 7: Scheme showing the setup for the FEM calculation of the relative length change for a single crystal of Terfenol-D along the crystallographic direction $\boldsymbol{\beta} = (cos(-\gamma), sin(-\gamma), 0)$ with magnetization along the crystallographic direction $\boldsymbol{\alpha} = (cos(\eta), sin(\eta), 0)$.

3.1.3. Magnetocrystalline anisotropy energy

The magnetocrystalline anisotropy energy for cubic crystal is given by Eq.10. In Fig. 9 we plot the magnetocrystalline anisotropy energy for single crystal Terfenol-D using K_1 and K_2 in Table 1. We see that the easy axis is along $< 111 >$, while the hard axis is $< 100 >$. The energy difference between hard and easy directions is $E_K^{001} - E_K^{111} = -K_1/3 - K_2/27 = 17\text{KJ/m}^3$. In Section 3.2.2 we will study how the orientation of the grains influences the magnetocrystalline anisotropy energy of polycrystalline Terfenol-D.

3.2. Polycrystal

3.2.1. Influence of grain morphology

To study the influence of grain morphology on elastic and magnetoelastic properties, we consider a material made of Terfenol-D with a rectangular geometry ($L_{x,0} = L_{y,0} = 10\mu$m and $L_{z,0} = 20\mu$m) and 3 types of microstructure: (i)

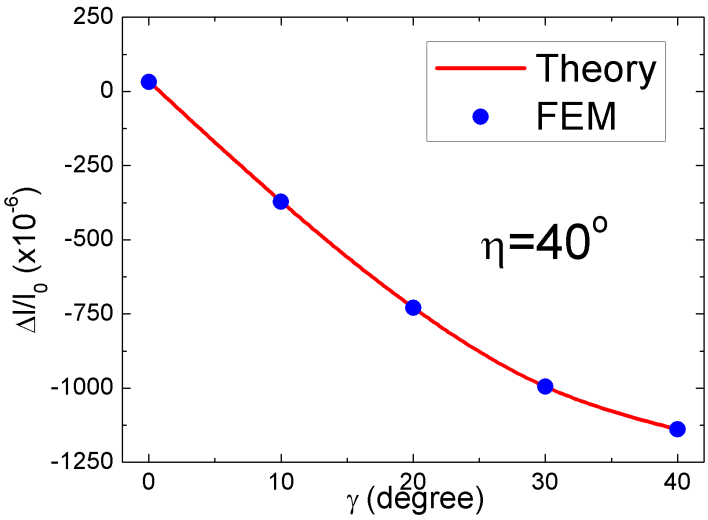

Figure 8: Calculation of the relative length change for a single crystal of Terfenol-D along the crystallographic direction $\boldsymbol{\beta} = (cos(-\gamma), sin(-\gamma), 0)$ when it is magnetized along the crystallographic direction $\boldsymbol{\alpha} = (cos(\eta), sin(\eta), 0)$ with $\eta = 40^o$. Blue dots and red line stand for FEM simulation and Eq.21, respectively.

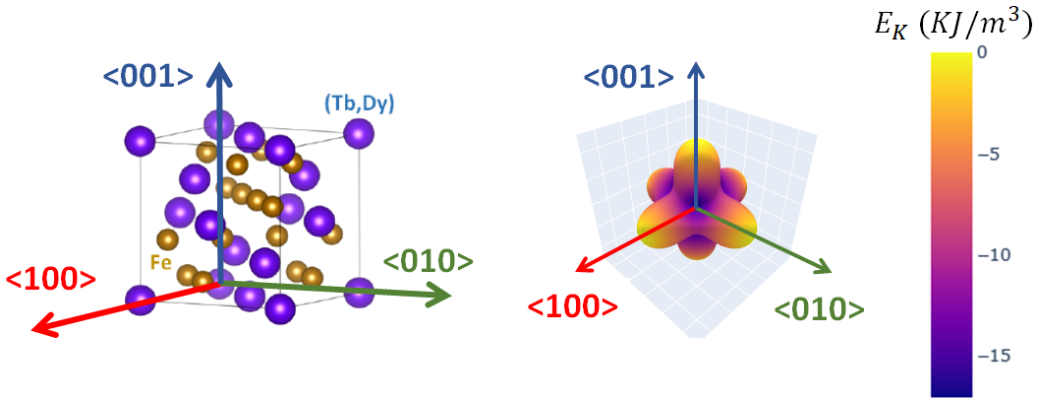

Figure 9: Magnetocrystalline anisotropy energy of single crystal Terfenol-D.

voronoi, (ii) columnar and (iii) multilayer, see Fig.10. For the voronoi and columnar microstructures we include 200 grains with uniformly-distributed orientations in 3D space [23], and we study two cases for each microstructure using a different seed in their generation with software Neper [22]. For the multilayer microstructure we include 50 layers with the same width (0.4μm), and we study two cases

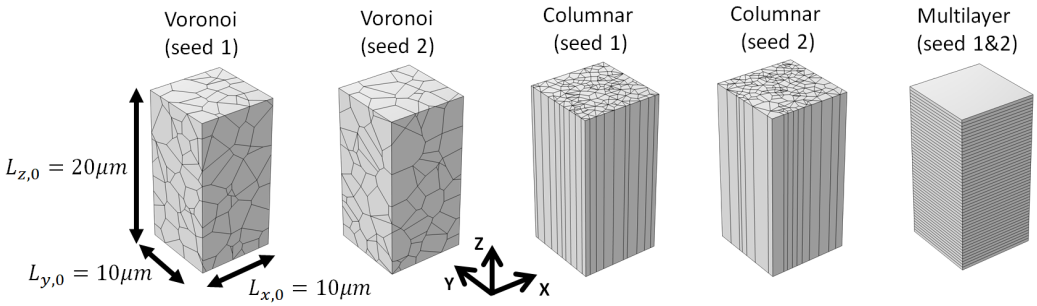

Figure 10: Polycrystalline models considered in this work to study the influence of grain morphology on elastic and magnetoelastic properties.

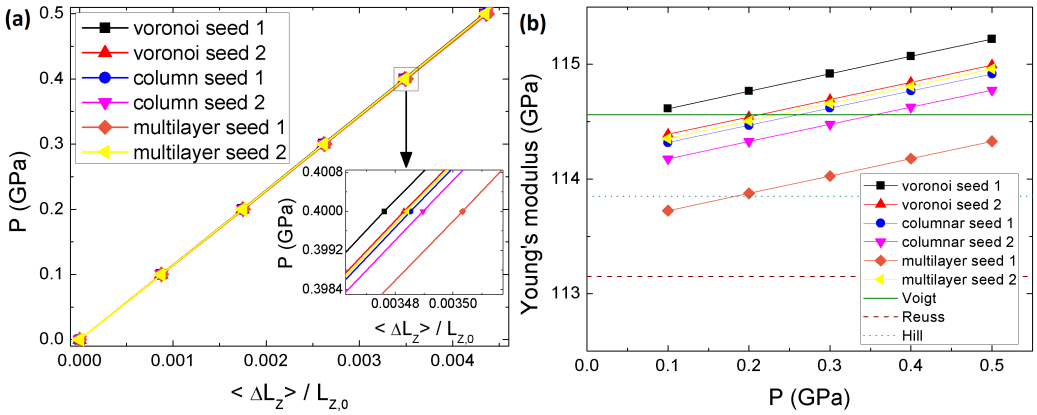

Figure 11: (a) Stress versus strain calculated with FEM simulations for different types of grain morphology and uniformly-distributed crystal orientations in 3D space. (b) Computed Young's modulus versus the applied stress. Horizontal lines stand for the theoretical values given by Voigt, Reuss and Hill averages derived from the elastic constants [26].

using the same morphology but with different uniformly-distributed crystal orientations of the layers. The methodology to compute the Young's modulus and magnetostriction is explained in Section 2.3. The calculated Young's modulus with FEM simulations for different types of grain morphology is shown in Fig.11. We observe that the computed Young's modulus decreases linearly as the applied pressure on the top and bottom boundaries is decreased. At low applied stress ($P \lesssim 0.1$GPa), the FEM results are found in between the theoretical values given by Voigt, Reuss and Hill averages [25, 26] derived from the elastic constants given by Table 1. These results are also close to the experimental value $Y = 110$ GPa [2]. In this linear elastic regime, we don't obtain a significant influence of grain

morphology on the Young's modulus. A more detailed view of the deformation for the voronoi microstructure (seed 1) is depicted in the Fig.12. In this figure, we also plotted the von Mises stress that can be used to analyze possible failures of the material under mechanical stress. We see that the highest values of von Mises stress are found close to some specific grain boundaries.

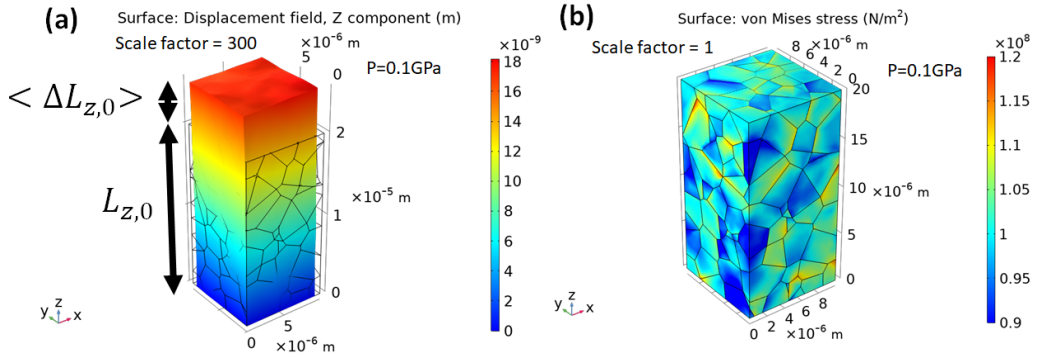

Figure 12: Calculated elastic response for the voronoi microstructure (seed 1) with uniformly-distributed crystal orientations in 3D space when external forces on the top and bottom boundaries ($P = 0.1$GPa) are applied along the z-axis direction. Surface color shows (a) the z-component of the displacement vector u_z and (b) von Mises stress. A scale factor 1000 is applied to (a) facilitate the visualization of the deformation.

Concerning the influence of grain morphology on magnetostriction, we computed the relative length change along z-axis direction versus the angle φ between the magnetization direction of all grains $\boldsymbol{m} = (sin\varphi, 0, cos\varphi)$ and z-axis direction, see Fig.13. We find that the FEM results for all models follow the relation [11, 27–29]

$$\left.\frac{\Delta l}{l_0}\right|_{\boldsymbol{\beta}'}^{\boldsymbol{m}} = \frac{3}{2}\lambda_S\left[(\boldsymbol{m}\cdot\boldsymbol{\beta}')^2 - \frac{1}{3}\right], \tag{22}$$

where λ_S is the isotropic magnetostrictive coefficient. For instance, since here we are computing the relative length change along z-axis direction, then we have $\boldsymbol{\beta}' = (0,0,1)$. In the theory of magnetostriction for polycrystalline materials, a widely used approximation is to assume that the stress distribution is uniform through the material. In this case the isotropic magnetostrictive coefficient reads [11, 27–29]

$$\lambda_S = \frac{2}{5}\lambda_{001} + \frac{3}{5}\lambda_{111}. \tag{23}$$

This result is analogous to the Reuss approximation used in the elastic theory of

Table 2: Isotropic magnetostrictive coefficient (λ_S) and Young's modulus (Y) calculated with FEM simulations for different types of microstructure with uniformly-distributed crystal orientations in 3D space. The FEM values for Y corresponds to the case with applied stress $P = 0.1$ GPa. The theoretical and experimental values are also shown for comparison. The theoretical value for λ_S is obtained via Eq.23 with the anisotropic magnetostrictive coefficients given in Table 1.

Approach	λ_S ($\times 10^{-6}$)	Y (GPa)	$Y\lambda_S$ (MPa)	$\frac{1}{2}Y\lambda_S^2$ (KJ/m^3)
FEM voronoi (seed 1)	1005	114.61	115.2	57.9
FEM voronoi (seed 2)	1022	114.39	116.9	59.7
FEM columnar (seed 1)	1011	114.32	115.6	58.4
FEM columnar (seed 2)	997	114.18	113.8	56.7
FEM multilayer (seed 1)	998	113.72	113.5	56.6
FEM multilayer (seed 2)	1040	114.35	118.9	61.8
Theory (Reuss)	996	113.15	112.7	56.1
Experiment	1080[a]	110[a]	118.8	64.2

[a]Ref.[2]

polycrystals to obtain a lower bound of Young's modulus [11, 26, 30, 31]. In Table 2 we present the results for λ_S calculated with FEM simulations for different types of microstructure with uniformly-distributed crystal orientations in 3D space. These values are obtained by fitting the data shown in Fig.13 to Eq.22. The theoretical and experimental values are also shown for comparison in Table 2. The theoretical value is obtained via Eq.23 with the anisotropic magnetostrictive coefficients given in Table 1. We see that Eq.23 gives a reasonable lower bound for λ_S ($\lambda_S = 996 \times 10^{-6}$) that is close to the experimental value $\lambda_S = 1080 \times 10^{-6}$ [2]. Similar to the Young's modulus, we don't see a significant influence of grain morphology on the λ_S. In Table 2 we also show the quantity $Y\lambda_S$, which is a measure of the pressure exerted by a constrained bar of the material which is magnetized to saturation [10]. Additionally, we include the energy density $\frac{1}{2}Y\lambda_S^2$ that represents the amount of magnetic energy which can be transformed to elastic energy per unit volume of the material [10]. A more detailed view of the magnetostrictive deformation for the voronoi microstructure (seed 1) is depicted in the Fig.14.

3.2.2. Influence of grain orientation

Elastic and magnetoelastic properties of polycrystalline materials can be tuned by orienting the growth of all grains along a specific crystallographic direction [3–5, 7]. In this section, we computationally explore how this effect influences

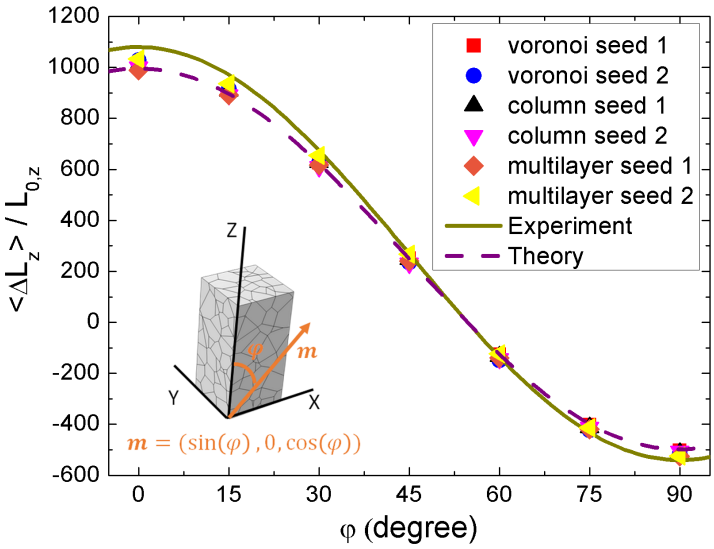

Figure 13: Relative length change along z-axis direction versus the angle φ between the magnetization direction of all grains $\boldsymbol{m} = (sin\varphi, 0, cos\varphi)$ and z-axis direction $\boldsymbol{\beta}' = (0,0,1)$. Symbols represent FEM simulations for different types of grain morphology and uniformly-distributed crystal orientations in 3D space. Solid and dash lines stand for Eq.22 using the experimental and theoretical value for λ_S, respectively.

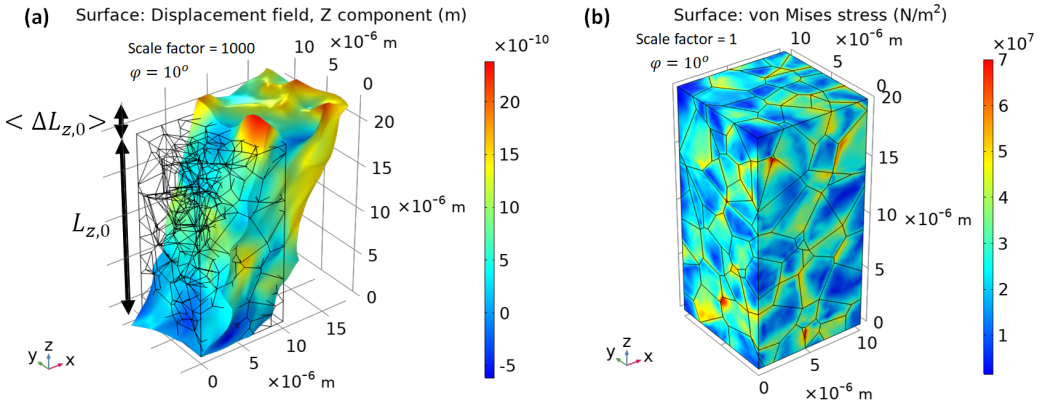

Figure 14: Calculated magnetostrictive response for the voronoi microstructure (seed 1) with uniformly-distributed crystal orientations in 3D space when magnetization of all grains is saturated along $\boldsymbol{m} = (sin\varphi, 0, cos\varphi)$ with $\varphi = 10^o$. Surface color shows (a) the z-component of the displacement vector u_z and (b) von Mises stress. A scale factor 1000 is applied to (a) facilitate the visualization of the deformation.

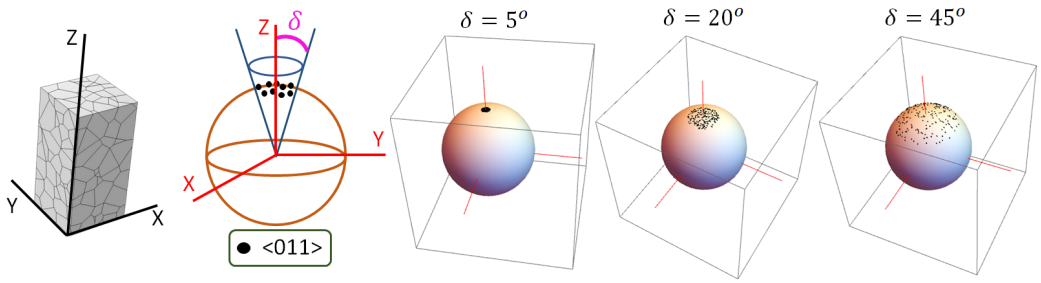

Figure 15: Uniformly distribution of crystallographic axis $< 011 >$ along the z-axis direction with dispersion angle $\delta = 5^o, 20^o, 45^o$.

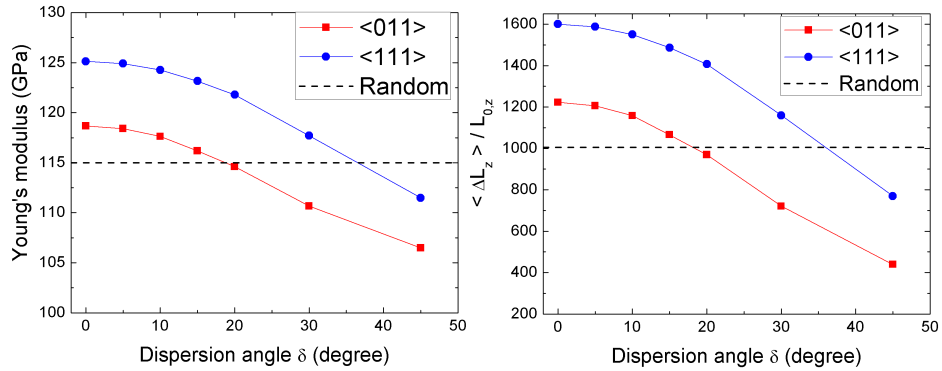

Figure 16: Computed (left) Young's modulus and (right) relative length change along the z-axis as a function of the dispersion angle δ for the FEM models with uniformly distribution of crystallographic axis $< 011 >$ and $< 111 >$ along the z-axis direction. Horizontal dash line stands for the result given by the FEM model using a uniformly distribution of the crystal orientations in all 3D space.

the Young's modulus, magnetostriction and magnetocrystalline anisotropy energy for Terfenol-D. For this analysis we consider the same voronoi microstructure (seed 1) than in Section 3.2.1, but now the crystallographic direction $< 011 >$ or $< 111 >$ of all grains will be uniformly oriented to the z-axis with a dispersion angle δ. The uniformly distribution of the crystallographic direction $< 011 >$ along the z-axis with a dispersion angle δ is achieved by setting the Euler angles

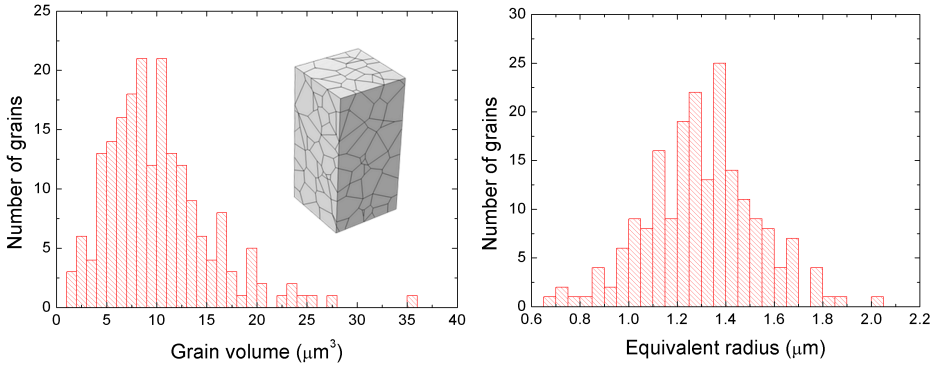

Figure 17: (Left) Hystogram of the grain volume V_0 of the polycrystalline model. Inset shows a picture of the corresponding microstructure. (Right) Hystogram of the equivalent radius (R_{eq}) assuming a spherical geometry of the grains $R_{eq} = [3V_0/(4\pi)]^{1/3}$.

to rotate each grain as [32]

$$\begin{aligned} |arccos(2v-1)| &< \delta, \\ \phi &= 0, \\ \theta &= \frac{\pi}{4} - |arccos(2v-1)|, \\ \psi &= 2\pi u, \end{aligned} \tag{24}$$

where v and u are random real numbers between 0 and 1. In Fig.15 we show the generated uniformly distribution of crystallographic axis $< 011 >$ along the z-axis direction with dispersion angle $\delta = 5^o, 20^o, 45^o$. Similarly, the uniformly distribution of the crystallographic direction $< 111 >$ along the z-axis with a dispersion angle δ is achieved by setting the Euler angles to rotate each grain as [32]

$$\begin{aligned} |arccos(2v-1)| &< \delta, \\ \phi &= \frac{\pi}{4}, \\ \theta &= \pi - arctan\left(\frac{1}{\sqrt{2}}\right) - |arccos(2v-1)|, \\ \psi &= 2\pi u. \end{aligned} \tag{25}$$

In Fig. 16 we present the computed Young's modulus and relative length change along the z-axis as a function of the dispersion angle δ for the FEM models with uniformly distribution of crystallographic axis $< 011 >$ and $< 111 >$ along the

z-axis direction. We see that distributions of the crystallographic axis $< 111 >$ with dispersion angle δ lower than 35^o exhibit larger Young's modulus and magnetostriction than an uniformly distribution of the crystal orientations in the all 3D space. For this case, we also observe that in the limit $\delta \to 0$ the relative length change tends to $\lambda_{111} = 1600 \times 10^{-6}$, as should be. We find that orienting the growth of all grains along crystallographic direction $< 011 >$ or $< 111 >$ with low dispersion angle can be a way to enhance the Young's modulus and magnetostriction of polycrystalline Terfenol-D. This fact could be particularly useful in the design of Terfenol-D for applications where the material must support large forces [2].

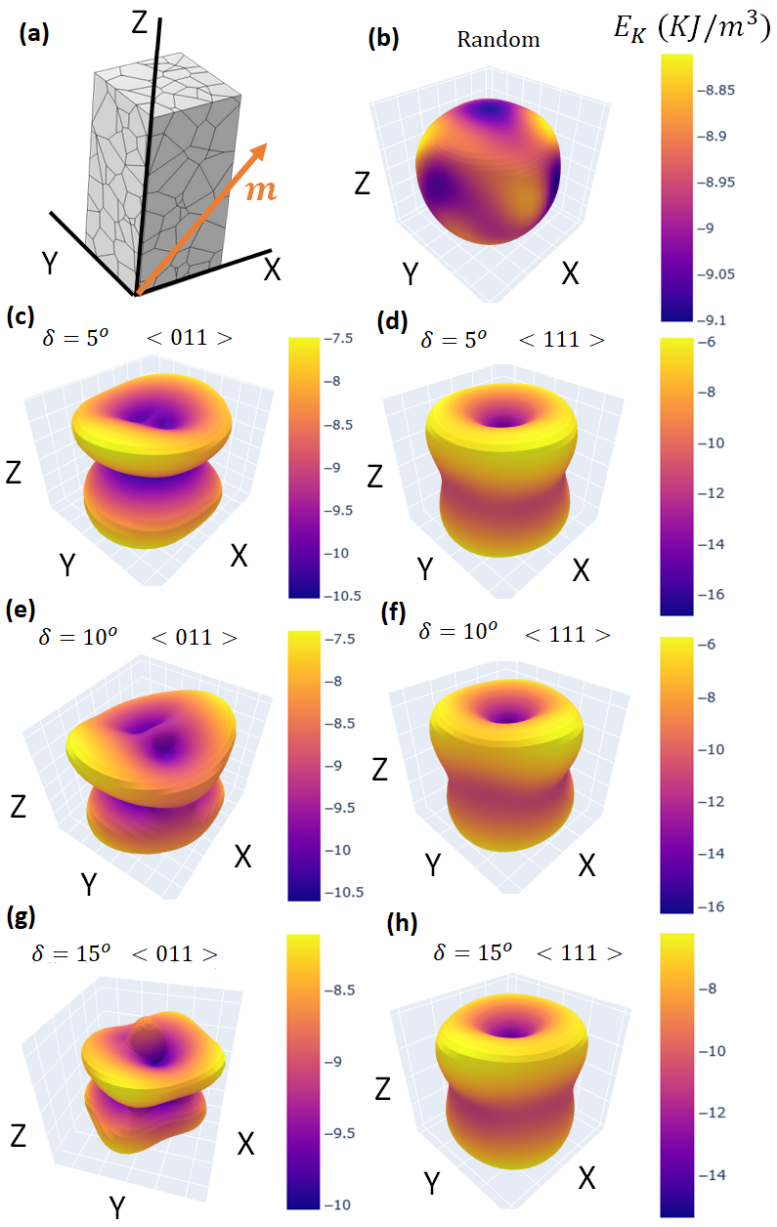

Figure 18: Magnetocrystalline anisotropy energy landscape of polycrystalline Terfenol-D. (a) Microstructure used in the model. (b) Polycrystalline model with random uniformly distribution of crystal orientations in the all 3D space. Polycrystalline model with uniformly distribution of crystallographic axis (c)(e)(g) $< 011 >$ and (d)(f)(h) $< 111 >$ along the z-axis direction for different values of the dispersion angle $\delta = 5^o, 10^o, 15^o$. Surface color represents the total magnetocrystalline anisotropy energy in units KJ/m^3.

Lastly, we analyze the magnetocrystalline anisotropy energy for the FEM models (voronoi microstructure, seed 1) with uniformly distribution of crystallographic axis $< 011 >$ and $< 111 >$ along the z-axis direction. The magnetocrystalline anisotropy energy of the all polycrystalline material is calculated in the following way. Firstly, we fix the magnetization of all grain along the same direction $\boldsymbol{m}$ (saturated state). Next, we compute $\boldsymbol{\alpha}$ using Eq. 9 for each grain. Additionally, we calculate the grain's volume ($V_{0,i}$) by performing FEM volume integration with the analysis tool of COMSOL, see Fig.17. Lastly, we evaluate the magnetocrystalline anisotropy energy of each grain through Eq. 10, and we sum the energy of all grains

$$\frac{E_{K,total}(\boldsymbol{m})}{V} = \frac{1}{V}\sum_{i=1}^{N} V_{0,i}E_{K,i}(\boldsymbol{m}) = \frac{1}{V}\sum_{i=1}^{N} V_{0,i}E_{K,i}(\boldsymbol{\alpha}_i), \tag{26}$$

where $V = L_{0,x}L_{0,y}L_{0,z}$ is the total volume and $N = 200$ is total number of grains. In Fig.18 we show the calculated magnetocrystalline anisotropy energy landscapes. We observe that the polycrystalline model with random uniformly distribution of crystal orientations in the all 3D space has energy barriers two order of magnitude lower than in the single crystal, so that it could be regarded as an approximately isotropic. Interestingly, we also see that an uniformly distribution of crystallographic axis $< 111 >$ along the z-axis direction with low dispersion angle δ leads to an effective uniaxial magnetocrystalline anisotropy that could be approximately described by

$$\frac{E_{K,total}(\boldsymbol{m})}{V} \simeq K_{0,eff} + K_{1,eff}(1-m_z^2) + K_{2,eff}(1-m_z^2)^2, \tag{27}$$

where $K_{0,eff}$, $K_{1,eff}$ and $K_{2,eff}$ are effective magnetocrystalline anisotropy constants. In Fig. 19 we show the fitting of the calculated energies to Eq.27. From this fitting we extract the values of $K_{0,eff}$, $K_{1,eff}$ and $K_{2,eff}$ which are also shown in Fig. 19 for different values of the dispersion angle δ. We observe that states with magnetization along the z-axis (easy axis) and in the XY plane (easy plane) exhibit high stability. According to the phase diagram of uniaxial magnetocrystalline anisotropy [33], this system could be considered as metastable because $K_{1,eff} > 0$, $K_{2,eff} < 0$ and $-K_{2,eff} < K_{1,eff} < -2K_{2,eff}$.

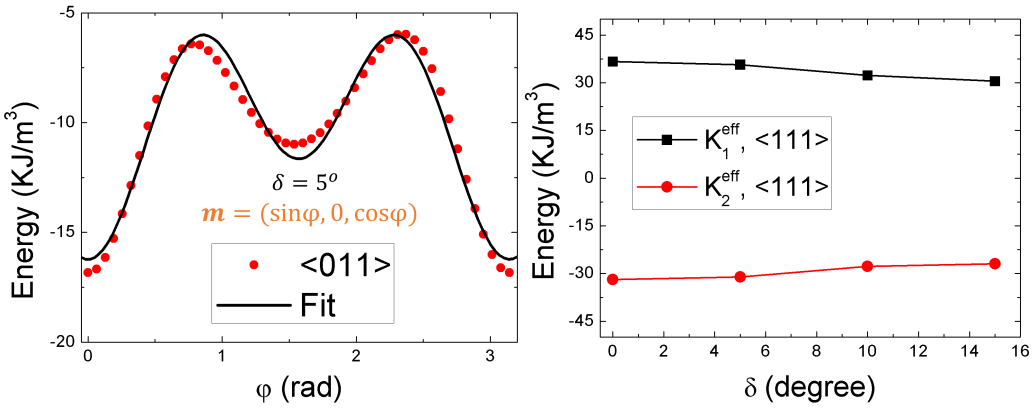

Figure 19: (Left) Magnetocrystalline anisotropy energy against the magnetization direction $\boldsymbol{m} = (sin\varphi, 0, cos\varphi)$ calculated for the polycrystalline model with uniformly distribution of crystallographic axis $< 111 >$ along the z-axis direction with dispersion angle $\delta = 5^o$ (red circles). Solid line stands for the fitting of the data to Eq.27. (Right) Fitted effective magnetocrystalline anisotropy constants for different values of the dispersion angle δ.

4. Conclusions

In summary, we studied the effect of microstructure on elastic and magnetostrictive properties of Terfenol-D by means of FEM. The simulations agree quite well with the theoretical and experimental Young's modulus and magnetostrictive coefficient of polycrystalline Terfenol-D. These properties are greatly influenced by the crystal orientation distribution of the grains, which gives a practical way to tune the performance of Terfenol-D. Interestingly, an effective macroscopic uniaxial magnetocrystalline anisotropy arises from the cubic crystal symmetry when the grains are uniformly oriented in crystal direction $< 111 >$ with low dispersion angle.

The presented approach could be useful to develop and validate theoretical models for describing elasticity, magnetostriction and magnetocrystalline anisotropy of polycrystalline materials [29, 30, 34]. Possible extensions of these models could incorporate a detailed description of grain boundaries suitable to study nanocrystalline alloys.

Similar methods as used here might also be applied to study the influence of microstructure and grain orientation on other physical properties given by anisotropic tensors [35] like thermal conductivity, piezoelectricity, optics and electrical conductivity.

Acknowledgement

This work was supported by the ERDF in the IT4Innovations national supercomputing center - path to exascale project (CZ.02.1.01/0.0/0.0/16-013/0001791) within the OPRDE. This work was supported by The Ministry of Education, Youth and Sports from the Large Infrastructures for Research, Experimental Development, and Innovations project "e-INFRA CZ - LM2018140". This work was supported by the Donau project No. 8X20050. DL acknowledge the Czech Science Foundations grant No. 20-18392S. P.N. and D.L acknowledge support from the H2020-FETOPEN no. 863155 s-NEBULA project.

References

[1] G. Engdahl, Handbook of giant magnetostrictive materials, Academic Press, 1999.

[2] M. Dapino, Encyclopedia of Smart Materials, John Wiley and Sons, Inc., New York, 2000.

[3] H. T. Savage, R. Abbundi, A. E. Clark, O. D. McMasters, Permeability, magnetomechanical coupling and magnetostriction in grain-oriented rare earth-iron alloys, Journal of Applied Physics 50 (B3) (1979) 1674–1676. arXiv:https://doi.org/10.1063/1.327234, doi:10.1063/1.327234.
URL https://doi.org/10.1063/1.327234

[4] B. W. Wang, L. Weng, S. Li, S. Zhou, I. Gyuro, Dynamic characteristics of tb-dy-fe polycrystals with <110> axial alignment, in: PRICM-5, Vol. 475 of Materials Science Forum, Trans Tech Publications Ltd, 2005, pp. 2251–2254. doi:10.4028/www.scientific.net/MSF.475-479.2251.

[5] O. Y. Kwon, H. Y. Kim, S. H. Hong, D. R. Son, Effect of texture on the magnetostriction of grain-aligned composite terfenol-d, Journal of Applied Physics 100 (12) (2006) 123905. arXiv:https://doi.org/10.1063/1.2402347, doi:10.1063/1.2402347.
URL https://doi.org/10.1063/1.2402347

[6] O. Y. Kwon, H. Y. Kim, S. I. Cha, S. H. Hong, Magnetostriction and magnetomechanical coupling of grain-aligned tb0.33dy0.67feyâ€‰/epoxy-filled composites, Journal of Applied Physics 97 (11) (2005) 113905. arXiv:https://doi.org/10.1063/1.1925335, doi:10.1063/1.1925335.
URL https://doi.org/10.1063/1.1925335

[7] C. Ji, J. Li, W. Ma, Y. Zhou, Preparation of terfenol-d with precise ã€^110ã€‰ orientation and observation of the oriented growth crystal morphology, Journal of Alloys and Compounds 333 (1) (2002) 291–295. doi:https://doi.org/10.1016/S0925-8388(01)01734-0.
URL https://www.sciencedirect.com/science/article/pii/S0925838801017340

[8] L. D. Landau, E. M. Lifshitz, Theory of elasticity / by L. D. Landau and E. M. Lifshitz ; translated from the Russian by J. B. Sykes and W. H. Reid, Pergamon London, 1959.

[9] B. A. Auld, Acoustic fields and waves in solids, Interscience, 1973.

[10] A. Clark, Chapter 7 magnetostrictive rare earth-Fe_2 compounds, Vol. 1 of Handbook of Ferromagnetic Materials, Elsevier, 1980, pp. 531 – 589. doi:10.1016/S1574-9304(05)80122-1.
URL http://www.sciencedirect.com/science/article/pii/S1574930405801221

[11] J. R. Cullen, A. E. Clark, K. B. Hathaway, Materials, science and technology, VCH Publishings, 1994, Ch. 16 - Magnetostrictive Materials, pp. 529–565.

[12] R. C. O'Handley, Modern magnetic materials, Wiley, 2000.

[13] C. Kittel, Physical theory of ferromagnetic domains, Rev. Mod. Phys. 21 (1949) 541–583. doi:10.1103/RevModPhys.21.541.
URL https://link.aps.org/doi/10.1103/RevModPhys.21.541

[14] G. F. Clark, B. K. Tanner, H. T. Savage, Synchrotron x-radiation topography studies of the magnetization process in tb0.27dy0.73fe2, Philosophical Magazine B 46 (4) (1982) 331–343. arXiv:https://doi.org/10.1080/13642818208246444, doi:10.1080/13642818208246444.
URL https://doi.org/10.1080/13642818208246444

[15] J.-F. Robillard, O. B. Matar, J. O. Vasseur, P. A. Deymier, M. Stippinger, A.-C. Hladky-Hennion, Y. Pennec, B. Djafari-Rouhani, Tunable magnetoelastic phononic crystals, Applied Physics Letters 95 (12) (2009) 124104. arXiv:https://doi.org/10.1063/1.3236537, doi:10.1063/1.3236537.
URL https://doi.org/10.1063/1.3236537

[16] J. Arnaudas, C. de la Fuente, M. Ciria, L. Benito, C. Dufour, K. Dumesnil, A. del Moral, Magnetoelastic stresses in epitaxial (110) terfenol-d thin films, Journal of Magnetism and Magnetic Materials 240 (1) (2002) 389–391, 4th International Symposium on Metallic Multilayers. doi:https://doi.org/10.1016/S0304-8853(01)00835-6.
URL https://www.sciencedirect.com/science/article/pii/S0304885301008356

[17] J. P. Teter, A. E. Clark, O. D. McMasters, Anisotropic magnetostriction in tb0.27dy0.73fe1.95, Journal of Applied Physics 61 (8) (1987) 3787–3789. arXiv:https://doi.org/10.1063/1.338646, doi:10.1063/1.338646.
URL https://doi.org/10.1063/1.338646

[18] T. Chookajorn, H. A. Murdoch, C. A. Schuh, Design of stable nanocrystalline alloys, Science 337 (6097) (2012) 951–954. arXiv:https://science.sciencemag.org/content/337/6097/951.full.pdf, doi:10.1126/science.1224737.
URL https://science.sciencemag.org/content/337/6097/951

[19] H. Kronmüller, M. Fähnle, Micromagnetism and the Microstructure of Ferromagnetic Solids, Cambridge University Press, 2003.

[20] https://comsol.com.

[21] MATLAB, version 9.9.0 (R2020b), The MathWorks Inc., Natick, Massachusetts, 2020.

[22] R. Quey, P. Dawson, F. Barbe, Large-scale 3d random polycrystals for the finite element method: Generation, meshing and remeshing, Computer Methods in Applied Mechanics and Engineering 200 (17) (2011) 1729–1745. doi:https://doi.org/10.1016/j.cma.2011.01.002.
URL https://www.sciencedirect.com/science/article/pii/S004578251100003X

[23] R. Quey, A. Villani, C. Maurice, Nearly uniform sampling of crystal orientations, Journal of Applied Crystallography 51 (4) (2018) 1162–1173. doi:10.1107/S1600576718009019.
URL https://doi.org/10.1107/S1600576718009019

[24] A. Marmier, Z. A. Lethbridge, R. I. Walton, C. W. Smith, S. C. Parker, K. E. Evans, Elam: A computer program for the analysis and representation of anisotropic elastic properties, Computer Physics Communications 181 (12) (2010) 2102–2115. doi:https://doi.org/10.1016/j.cpc.2010.08.033.
URL https://www.sciencedirect.com/science/article/pii/S0010465510003401

[25] R. Gaillac, P. Pullumbi, F.-X. Coudert, ELATE: an open-source online application for analysis and visualization of elastic tensors, Journal of Physics: Condensed Matter 28 (27) (2016) 275201. doi:10.1088/0953-8984/28/27/275201.
URL https://iopscience.iop.org/article/10.1088/0953-8984/28/27/275201

[26] S. Zhang, R. Zhang, AELAS: Automatic ELAStic property derivations via high-throughput first-principles computation, Computer Physics Communications 220 (2017) 403 – 416. doi:10.1016/j.cpc.2017.07.020.
URL http://www.sciencedirect.com/science/article/pii/S0010465517302400

[27] N. S. Akulov, Z. Physik 52, 389 (1928).

[28] E. W. Lee, Magnetostriction and magnetomechanical effects, Reports on Progress in Physics 18 (1) (1955) 184–229. doi:10.1088/0034-4885/18/1/305.

[29] R. Birss, The saturation magnetostriction of ferromagnetics, Advances in Physics 8 (31) (1959) 252–291. arXiv:https://doi.org/10.1080/00018735900101198, doi:10.1080/00018735900101198.
URL https://doi.org/10.1080/00018735900101198

[30] A. Reuss, Berechnung der Fließgrenze von Mischkristallen auf Grund der Plastizitätsbedingung für Einkristalle, ZAMM - Journal of Applied Mathematics and Mechanics 9 (1) (1929) 49–58. arXiv:https://onlinelibrary.wiley.com/doi/pdf/10.1002/zamm.19290090104, doi:10.1002/zamm.19290090104.
URL https://onlinelibrary.wiley.com/doi/abs/10.1002/zamm.19290090104

[31] R. Hill, The elastic behaviour of a crystalline aggregate, Proceedings of the Physical Society. Section A 65 (5) (1952) 349–354. doi:10.1088/0370-1298/65/5/307.

[32] E. W. Weisstein, Sphere Point Picking. From Mathworld - A Wolfram Web Resource, https://mathworld.wolfram.com/SpherePointPicking.html.

[33] J. M. D. Coey, Magnetism and Magnetic Materials, Cambridge University Press, New York, 2009.

[34] G. Asti, S. Rinaldi, Singular points in the magnetization curve of a polycrystalline ferromagnet, Journal of Applied Physics 45 (8) (1974) 3600–3610. arXiv:https://doi.org/10.1063/1.1663823, doi:10.1063/1.1663823.
URL https://doi.org/10.1063/1.1663823

[35] D. R. Lovett, Tensor Properties of Crystals, Second Edition, CRC Press, 2018. doi:10.1201/9780203737286.
URL https://doi.org/10.1201%2F9780203737286